

# PRECIPITATION MODEL VALIDATION IN 3<sup>RD</sup> GENERATION AEROTURBINE DISC ALLOYS

G.B. Olson<sup>1,2</sup>, H.-J. Jou<sup>1</sup>, J. Jung<sup>1</sup>, J.T. Sebastian<sup>1</sup>, A. Misra<sup>1</sup>, I. Locci<sup>3</sup> and D. Hull<sup>3</sup>

<sup>1</sup>QuesTek Innovations LLC, Evanston, IL 60201, USA, email: hjjou@questek.com

<sup>2</sup>Northwestern University, Evanston IL, 60208, USA

<sup>3</sup>NASA Glenn Research Center, Cleveland, OH 44135, USA

Keywords: Precipitation, Nickel-Based Superalloys, CALPHAD, Thermodynamics, Diffusion, Precipitation, Modeling

## Abstract

In support of application of the DARPA-AIM methodology to the accelerated hybrid thermal process optimization of 3<sup>rd</sup> generation aeroturbine disc alloys with quantified uncertainty, equilibrium and diffusion couple experiments have identified available fundamental thermodynamic and mobility databases of sufficient accuracy. Using coherent interfacial energies quantified by Single-Sensor DTA nucleation undercooling measurements, *PrecipiCalc*<sup>TM</sup> simulations of nonisothermal precipitation in both supersolvus and subsolvus treated samples show good agreement with measured  $\gamma'$  particle sizes and compositions. Observed long-term isothermal coarsening behavior defines requirements for further refinement of elastic misfit energy and treatment of the parallel evolution of incoherent precipitation at grain boundaries.

## Introduction

An important ongoing application of predictive science-based computational materials engineering is the accelerated hybrid process optimization of dual microstructure aeroturbine discs fabricated from 3<sup>rd</sup> generation high-refractory Ni-base superalloys. In support of higher fidelity application of the DARPA-AIM methodology previously demonstrated on the IN100 and R88DT disc alloys [1,2], a collaborative model and database validation study is supported by the NASA Aviation Safety Program to better quantify uncertainty and improve prediction accuracy of the QuesTek *PrecipiCalc* multiphase/multicomponent precipitation simulation code developed as the primary engine of the AIM methodology.

Table 1 Nominal compositions (balance Ni) of the four 3<sup>rd</sup> generation disc alloys studied under this program.

		Cr	Co	Mo	W	Al	Ti	Nb	Ta	Hf	C	B	Zr
ME3	wt%	13.1	20.0	3.8	1.9	3.5	3.6	1.1	2.3	-	0.04	0.03	0.05
	at%	14.5	19.5	2.3	0.6	7.5	4.3	0.7	0.7	-	0.19	0.16	0.03
LSHR	wt%	13.0	21.0	2.7	4.3	3.5	3.5	1.5	1.6	-	0.03	0.03	0.05
	at%	14.5	20.7	1.6	1.4	7.5	4.2	0.9	0.5	-	0.15	0.16	0.03
Alloy10	wt%	10.2	14.9	2.7	6.2	3.7	3.9	1.9	0.9	-	0.03	0.03	0.10
	at%	11.5	14.8	1.6	2.0	8.0	4.8	1.2	0.3	-	0.15	0.16	0.07
RR1000	wt%	15.0	18.5	5.0	-	3.0	3.6	-	2.0	0.5	0.03	0.015	0.06
	at%	16.5	17.9	3.0	-	6.4	4.3	-	0.6	0.2	0.13	0.080	0.04

Four 3<sup>rd</sup>-generation nickel-based disk superalloys, including ME3 (also called René104), LSHR (Low-Solvus, High-Refractory alloys developed by NASA), Alloy 10 (developed by Honeywell), and RR1000 (developed by Rolls-Royce) are being studied under this program, and their nominal compositions are listed in Table 1. In the following sections, key results from the 1<sup>st</sup> year of this NASA/QuesTek collaboration are provided.

## *PrecipiCalc* Calibration and Validation Protocol

An initial objective of this NASA program is to develop a standard *PrecipiCalc* calibration and validation protocol for intragranular  $\gamma'$  precipitation. The protocol needs to employ independent experimental measurements to decouple and/or minimize the cross interaction between model parameters, allowing the determination of the model parameters with high fidelity and minimum overfitting. The protocol must sequentially address the foundational databases and model parameters of the *PrecipiCalc* method, which include:

- CALPHAD fundamental databases — *PrecipiCalc* relies on CALPHAD-based databases to capture fundamental mechanistic features of multicomponent alloys. These databases and associated tuning parameters include:
  - Thermo-Calc<sup>®</sup> [3] compatible thermodynamic databases — representing bulk free energy with state variables such as composition and temperature;
  - $\Delta E$  — a phase free energy shift in Thermo-Calc to locally tune equilibrium phase fractions;
  - DICTRA [4] compatible mobility databases — representing atomic mobility and allowing calculation of diffusivity when combined with the thermodynamic database;
  - $D_{\text{scale}}$  — diffusivity correction factor used by *PrecipiCalc* to easily rescale the diffusivity matrix for local fitting;
  - Molar Volume — preliminary multicomponent molar volume models were developed for both  $\gamma$  and  $\gamma'$  under the AIM program
- Material kinetic model parameters:
  - $\sigma_{\text{coh}}$  — coherent surface energy, which is the key parameter affecting the nucleation barrier when particles are small and coherent with the surrounding matrix;
  - $G_{\text{el}}$  — elastic coherency (misfit) energy adds additional energy penalty to the precipitation when the particles are coherent with the matrix;
  - $\sigma_{\text{incoh}}$  — incoherent surface energy captures the increased surface energy when the particles lose coherency with the matrix;
  - $M_0$  — prefactor for the interfacial mobility term to describe incoherent interfaces, while the corresponding activation energy is scaled to that for solvent self diffusion;
  - $R_{\text{coh} \rightarrow \text{incoh}}$  — the characteristic particle size for coherency transition.

The current *PrecipiCalc* calibration and validation protocol is summarized in Table 2. High-temperature long aging is applied to Ni-based superalloys to produce near equilibrium microstructures, and matrix/particle compositions are measured by APT and EDS, (see next section). The results help down-select a candidate

thermodynamic database and determine potential simple energy corrections  $\Delta E$ . Next, diffusion couples between Ni-based superalloys and pure Ni with high temperature aging are used to determine if there is a need to correct mobility of individual components or scale with a simple scaling factor ( $D_{\text{scale}}$ ) to the calculated diffusivity from databases. Ultimately, XRD can be used to evaluate the importance of misfit and modify the molar volume models if needed.

Table 2 Summary of calibration and validation protocol.

Experiments	CALPHAD Fundamental Databases	Material Kinetic Model Parameters
Equilibrium Age + APT and EDS Compositions	Thermodynamics, $\Delta E$	
Diffusion Couple + Microanalysis	Mobility, $D_{\text{scale}}$	
SSDTA + APT		$\sigma_{\text{coh}}$ , $G_{\text{el}}$ (est.)
Coarsening Age + SEM/TEM for $\gamma'$ size and fraction		$\sigma_{\text{incoh}}$ , $M_0$
XRD, TEM for misfit	Molar Volume	$G_{\text{el}}$ , $R_{\text{coh} \rightarrow \text{incoh}}$

For material specific model parameters of precipitation kinetics, nonisothermal nucleation experiments using SSDTA (see later discussion) were identified to determine coherent  $\gamma'$  surface energy ( $\sigma_{\text{coh}}$ ) and estimated elastic coherency energy ( $G_{\text{el}}$ ). Next, later stage coarsening experiments are used to determine the incoherent  $\gamma'$  surface energy ( $\sigma_{\text{incoh}}$ ) and possible interfacial mobility term ( $M_0$ ). Finally, TEM study can be used to determine the coherency transition size ( $R_{\text{coh} \rightarrow \text{incoh}}$ ), and to assist the calculation of elastic coherency energy ( $G_{\text{el}}$ ).

### Thermodynamics

To assess equilibrium phase fractions and compositions, water quenched supersolvus treated samples of ME3, LSHR, Alloy10 and RR1000 disc alloys are given 1000hr treatments at temperatures of 1093°C (2000°F), 927°C (1700°F), and 760°C (1400°F). Commercial thermodynamic databases compared in this study, using Thermo-Calc [3] software, include Thermotech Ni-DATA versions 4 to 7 [5], Computherm PanNickel [6], Ni-NIST [7] (not including Nb), and TCNI1 [8] (not including Mo, Nb and Ta).

### Alloy 10/ME3 Equilibrium Studies

Comparison in equilibrium phase compositions was undertaken with evaluation of the Alloy10 and ME3 samples quenched from the 1093°C 1000hr age treatment. The high-temperature matrix composition of ME3 was determined by both Energy Dispersive Spectroscopy (EDS) analysis conducted at NASA GRC and Atom-Probe Tomography (APT) using an Imago Local Electrode Atom Probe (LEAP) with new larger-FOV LEAP detector at the Northwestern University Center for Atom Probe Tomography (NUCAPT). In addition,  $\gamma'$  composition was also successfully measured by EDS for both alloys.

A LEAP dataset with 2.2 million atoms and dimensions of 36×37×60 nm<sup>3</sup> was analyzed for the ME3 sample. No large isothermally aged  $\gamma'$  was detected in LEAP (the fine  $\gamma'$  formed during quench will be discussed later), and thus the entire LEAP dataset represents the matrix during the high temperature age. Table 3 summarizes both the quantitative APT and semi-quantitative EDS results, and a comparison with the predicted high temperature matrix compositions using different thermodynamics databases. Based on the root mean square (RMS) error of solute content relative to the APT measurement, the Ni-DATA 7 database gives the best agreement. In the last column of Table 3, an experimental phase fraction of 24.8% was estimated by mass balance using the APT measured matrix composition and the Ni-DATA 7 predicted  $\gamma'$  composition, and again the Ni-DATA 7 prediction provides the best agreement. The comparison of predicted versus EDS measured  $\gamma'$  compositions also confirm the best agreement from the Ni-DATA 7 database.

Table 3 Comparison of the predicted  $\gamma$  and  $\gamma'$  compositions and  $\gamma'$  phase fraction in ME3 at 1093°C (2000°F) with the experimental APT  $\gamma$  and EDS  $\gamma$  and  $\gamma'$  compositions. Ni-DATA version 5 (or 7) is abbreviated as Ni 5 (or 7) in the table.

		Composition at 1093°C, at%											% $\gamma'$ fraction
		Ni	Al	Cr	Co	Ti	Mo	W	Nb	Ta	C	RMS	
$\gamma$	APT	44.9	6.7	17.5	21.7	3.5	3.4	1.0	0.5	0.5	0.04		24.8
	2 $\sigma$	0.04	0.02	0.03	0.03	0.01	0.01	0.01	0.01	0.01	0.002		1.5
	EDS	46.1	6.6	16.6	22.7	3.3	3.0	1.3*	0.6	-	-		
	Ni 5,6	45.7	5.6	19.7	22.1	2.4	3.1	0.7	0.3	0.3	0.01	0.93	30.7
	<b>Ni 7</b>	<b>46.4</b>	<b>6.0</b>	<b>18.5</b>	<b>21.8</b>	<b>2.7</b>	<b>3.0</b>	<b>0.7</b>	<b>0.4</b>	<b>0.5</b>	<b>0.01</b>	<b>0.54</b>	25.5
	Pan-Nickel	44.3	5.3	20.3	23.0	2.4	2.9	0.8	0.4	0.5	0.05	1.19	32.3
$\gamma'$	NIST-Ni	44.7	5.1	19.9	23.8	2.4	3.2	0.8		0.2		1.44	29.4
	EDS	58.4	12.9	4.1	12.8	8.9	0.5	0.3	0.6	1.4	-		
	Ni 5,6	61.5	5.7	2.6	14.4	7.1	0.5	0.9	2.4	4.9	-	3.09	
	<b>Ni 7</b>	<b>60.2</b>	<b>12.0</b>	<b>2.8</b>	<b>13.0</b>	<b>8.8</b>	<b>0.3</b>	<b>0.3</b>	<b>1.3</b>	<b>1.2</b>	-	<b>0.63</b>	
	Pan-Nickel	61.8	12.3	2.2	12.5	8.2	0.4	0.1	1.2	1.1	-	0.81	
	NIST-Ni	68.3	6.3	1.3	9.7	7.6	0.3	0.3	-	6.2	-	3.27	

\* value includes both W and Ta due to peak overlaps in EDS.

High temperature  $\gamma$  and  $\gamma'$  compositions of Alloy 10 (1093°C 1000hr) were successfully measured by EDS, and compared with several thermodynamic databases in Table 4. Combined W+Ta composition is reported for EDS due to peak overlap. Overall, Ni-DATA 7 agrees the best with the semi-quantitative EDS measurement.

A systematic underestimation of Ti in the calculated  $\gamma$  matrix was also noted in QuesTek's earlier simulations in the DARPA-AIM initiative on commercial Ni-base superalloys [1] and may have to be addressed later in this program.

Table 4 Comparison of the predicted  $\gamma$  and  $\gamma'$  compositions at 1093°C and EDS measurement for Alloy 10 aged at 1093°C for 1000 hr.

		Compositions, at%									
		Ni	Al	Cr	Co	Ti	Mo	W	Ta	Nb	RMS
$\gamma$	EDS	53.8	7.0	13.4	17.5	3.2	2.3	1.6	1.13		
	Ni 5,6	50.8	5.74	17.60	17.76	2.61	2.30	2.54	0.14	0.50	1.75
	Ni 7	51.1	5.97	16.97	17.72	2.76	2.21	2.48	0.20	0.63	1.49
	Ni-NIST	51.3	5.44	17.00	18.60	2.58	2.31	2.66	0.10	-	1.68
$\gamma'$	EDS	62.3	13.0	4.0	10.9	7.2	0.6	0.9	1.3		
	Ni 5,6	62.2	12.02	2.82	11.01	8.42	0.24	0.93	0.49	1.89	0.80
	Ni 7	64.1	12.11	2.80	10.53	8.64	0.23	0.91	0.40	1.73	0.83
	Ni-NIST	66.8	13.5	1.35	7.54	9.62	0.13	0.37	0.68	-	1.93

#### Ni-Al-Cr(-X) (X=Re,W) Model Alloys

Table 5 Phase composition comparison of APT [9] and the database predictions for a Ni-5.2Al-14.2Cr (at%) alloy at 600°C.

600°C			at%				APB	600°C	% $\gamma'$
			Ni	Al	Cr	RMS	(J/m <sup>2</sup> )	misfit %	fraction
$\gamma$	Equilibrium matrix composition	APT	81.26	3.13	15.61				
		2 $\sigma$	0.18	0.08	0.18	0.14			
		Ni 5,6	81.40	3.64	14.96	0.58			
		<b>Ni 7</b>	<b>81.34</b>	<b>3.62</b>	<b>15.04</b>	<b>0.53</b>			
		TCNI1	81.17	3.93	14.90	0.76			
		Ni-NIST	80.60	5.20	14.20	1.77			
$\gamma'$	$\gamma'$ equilibrium composition	APT	76.53	16.69	6.77		0.19	-0.72	15.4
		2 $\sigma$	0.50	0.44	0.30	0.38	0.01		0.4
		Ni 5,6	74.98	16.23	8.80	1.47	0.19	-0.6	12.4
		<b>Ni 7</b>	<b>74.97</b>	<b>16.21</b>	<b>8.82</b>	<b>1.49</b>	0.19	-0.6	12.4
		TCNI1	75.59	14.55	9.57	2.49	0.18	-0.8	12.3
		Ni-NIST	75.96	12.25	11.79	4.74	0.15	-0.9	0.0
	Critical $\gamma'$ -nucleus composition	APT	72.40	18.30	9.30		0.16	-0.2	
		2 $\sigma$	2.20	1.80	1.40	1.61	0.03		
		Ni 5,6	74.91	17.37	7.71	1.30	0.20	-0.5	
		<b>Ni 7</b>	<b>74.91</b>	<b>17.40</b>	<b>7.69</b>	<b>1.30</b>	0.20	-0.5	
		TCNI1	75.36	16.43	8.21	1.53	0.20	-0.6	
		Ni-NIST	No precipitation						

Further comparison of thermodynamic databases is enabled by previous APT and ICP (Inductively Coupled Plasma atomic-emission spectroscopy measurement) studies at Northwestern University of isothermal  $\gamma'$  precipitation in simple Ni-Al-Cr-X model alloys [9-13]. The measured time evolution of particle size suggests the precipitation composition trajectory can be modeled as an unstable equilibrium with capillarity. Comparison of phase compositions with the database predictions for these alloys is made in Tables 5-8. For the base Ni-Al-Cr alloy at 600°C, measurement of the composition trajectory includes the initial critical nucleus composition. As metrics of relative impact of phase composition error, Tables 5-8 include not only the RMS solute concentration error and  $\gamma'$  phase fraction, but the corresponding predicted error in thermodynamically computed  $\gamma'$  APB enthalpy [13], and the at-temperature interphase lattice-

parameter misfit based on QuesTek's molar volume model. These comparisons again support the Ni-DATA 7 database as most accurate, and suggest the corresponding error in APB enthalpy and misfit is acceptable within current structure/property model uncertainty.

While predicted phase fractions show good agreement with experiment for the complex superalloy of Table 3, we note a significant discrepancy for the simpler model alloys of Tables 5-8. For these alloys a  $\Delta E$  shift in the relative free energy of  $\gamma'$  could be appropriate for further modeling of precipitation dynamics.

Table 6 Phase composition comparison of ICP [10] and the database predictions for a Ni-10Al-8.5Cr (at%) alloy at 800°C.

800°C		at%				% $\gamma'$
		Ni	Al	Cr	RMS	fraction
$\gamma$ equilibrium matrix composition	ICP	82.71	8.43	8.86		
	2 $\sigma$	0.24	0.16	0.18	0.17	
	Ni 5,6	82.93	8.32	8.75	0.11	
	<b>Ni 7</b>	<b>82.93</b>	<b>8.32</b>	<b>8.75</b>	<b>0.11</b>	
$\gamma'$ equilibrium precipitate composition	Ni-NIST	81.90	9.76	8.34	1.01	
	ICP	76.60	17.41	5.99		14.6
	2 $\sigma$	0.36	0.34	0.12	0.25	0.3
	Ni 5,6	75.52	18.64	5.84	0.88	13.9
	<b>Ni 7</b>	<b>75.52</b>	<b>18.64</b>	<b>5.84</b>	<b>0.88</b>	13.9
	Ni-NIST	76.47	17.40	6.13	0.10	0.0

Table 7 Phase composition comparison of APT [11] and the database predictions for a Ni-Al-Cr-Re alloy at 800°C.

800°C			at%					APB	800°C	% $\gamma'$
			Ni	Cr	Al	Re	RMS	(J/m <sup>2</sup> )	misfit %	fraction
$\gamma$	Equilibrium matrix composition	APT	81.07	10.04	6.74	2.15				
		2 $\sigma$	0.16	0.04	0.08	0.02	0.05			
		<b>Ni 7</b>	<b>80.55</b>	<b>8.94</b>	<b>8.35</b>	<b>2.16</b>	<b>1.13</b>			
		Ni-NIST	80.22	8.79	8.87	2.12	1.42			
$\gamma'$	Equilibrium composition	APT	76.17	4.97	18.05	0.81		0.19	-0.71	24.8
		2 $\sigma$	0.26	0.10	0.18	0.04	0.12	0.00		0.2
		<b>Ni7</b>	<b>75.29</b>	<b>5.68</b>	<b>18.80</b>	<b>0.23</b>	<b>0.68</b>	0.20	-0.68	15.9
		Ni-NIST	75.82	6.13	17.65	0.39	0.75		-0.77	7.2
	composition at 80% completion	APT	76.33	5.46	16.92	1.29		0.17		20.3
		2 $\sigma$	0.30	0.16	0.26	0.08	0.18	0.00		0.2
		<b>Ni7</b>	<b>75.22</b>	<b>5.56</b>	<b>18.99</b>	<b>0.23</b>	<b>1.35</b>	0.20		12.8
		Ni-NIST								

Table 8 Phase composition comparison of APT [12] and the database predictions for a Ni-Al-Cr-W alloy at 800°C.

800°C		at%					APB	800°C	% $\gamma'$
		Ni	Cr	Al	W	RMS	(J/m <sup>2</sup> )	misfit %	fraction
$\gamma'$ equilibrium matrix composition	APT	81.31	5.83	11.52	1.34				
	2 $\sigma$	0.07	0.04	0.05	0.02	0.04			
	Ni 7	81.44	6.22	10.53	1.80	0.67			
	Ni-NIST	80.48	8.57	8.84	2.11	2.26			
$\gamma'$ equilibrium precipitate composition	APT	76.30	17.00	3.91	2.80		0.21	-0.49	37.9
	2 $\sigma$	0.08	0.07	0.04	0.03	0.05	0.00		0.0
	Ni7	75.39	18.00	4.20	2.42	0.64	0.22	-0.36	32.1
	Ni-NIST	75.87	16.61	6.42	1.09	1.77		-0.61	18.7

### Misfit Estimates

Comparison of relative interphase misfit also provides a useful metric of database accuracy for the complex disc alloys. Figure 1 summarizes the predicted equilibrium at-temperature  $\gamma/\gamma'$  misfit for disc alloys, taking into account the presence of equilibrium carbides, using phase compositions predicted by the Ni-DATA 7 database. The alloys fall into 2 groups of relatively high and low misfit. Of the 3<sup>rd</sup> generation disc alloys, only the RR1000 alloy is predicted to maintain the low misfit of the IN100 and René88DT alloys. In support of this prediction, Figure 2 compares the  $\gamma'$  microstructures of supersolvus treated (1193°C/1hr) Alloy10 and RR1000 after long-term aging at 1093°C for 1000 hr. While the fine intragranular precipitates in Alloy10 show the cuboidal morphology and ordered arrays consistent with the predicted higher misfit, the  $\gamma'$  in RR1000 shows a spheroidal morphology and disordered spatial distribution consistent with its predicted low misfit. The combination of thermodynamic database and misfit model thus appears to give a reasonable ranking of relative misfit between alloys. However, the higher misfit values appear surprisingly large and XRD studies are planned to calibrate the molar volume model. Elastic energy based misfit estimates from relative nucleation undercoolings are discussed later.

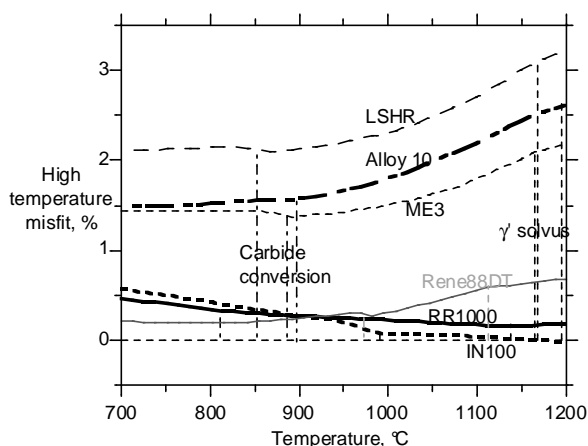


Figure 1 Summary of predicted equilibrium at-temperature  $\gamma/\gamma'$  misfit for disc alloys, taking into account the presence of equilibrium carbides, using phase compositions predicted by the Ni-DATA 7 database and the preliminary molar volume model.

### Mobility

To assess accuracy of available atomic mobility databases for combination with thermodynamic databases in order to predict multicomponent diffusivities, a linear diffusion “multiple” was prepared at NASA GRC. A 5mm (0.2-inch) thick disc of pure Ni was diffusion bonded by hot pressing to a 3.2mm (0.125-inch) thick disc of ME3 on one side and to a 3.2mm (0.125-inch) thick disc of Alloy 10 on the other, for 4 hours at 877°C (1610 °F) in vacuum. After the initial bond was formed, the diffusion couple was subjected to additional annealing in a horizontal tube furnace in an argon atmosphere at two temperatures, 1093°C or 927°C for 100 or 300 hours.

DICTRA [4] simulations with Ni-DATA 7 and the NIST mobility database [14] of the diffusion multiple at the hot-pressing temperature 877°C predicted no significant diffusion. Therefore, subsequent simulations ignored the hot-pressing step.

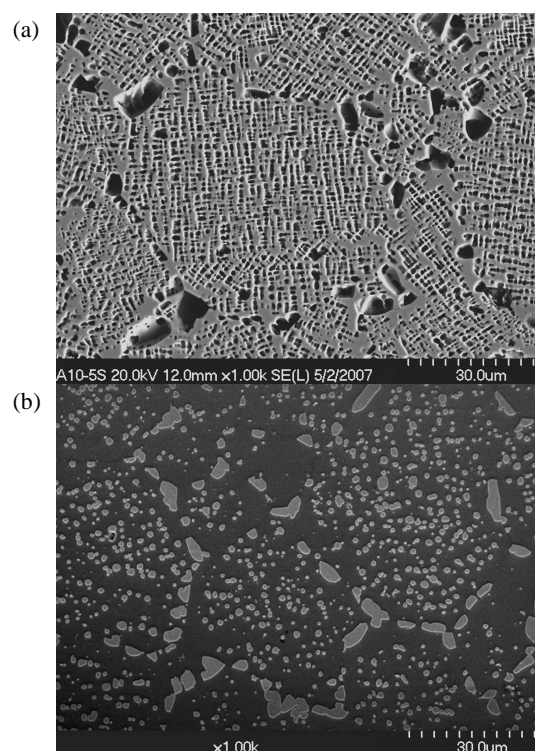


Figure 2 Comparison of the  $\gamma'$  microstructures of (a) Alloy 10 and (b) RR1000 (courtesy of L. Birrell at University of Cambridge)

Next, the NIST mobility database employed in the AIM project was compared with the Thermo-Calc MOB1 database in combination with various thermodynamic databases. In order to compare microprobe analyses of the diffusion multiple with DICTRA simulations, the average Matano interface (defined as the interface across which equal number of atoms have crossed in both directions) was equated to the origin of the calculated profiles, and simulations assumed that  $\gamma'$  precipitates act only as sink or source of solute for diffusion, i.e. no diffusion through  $\gamma'$ .

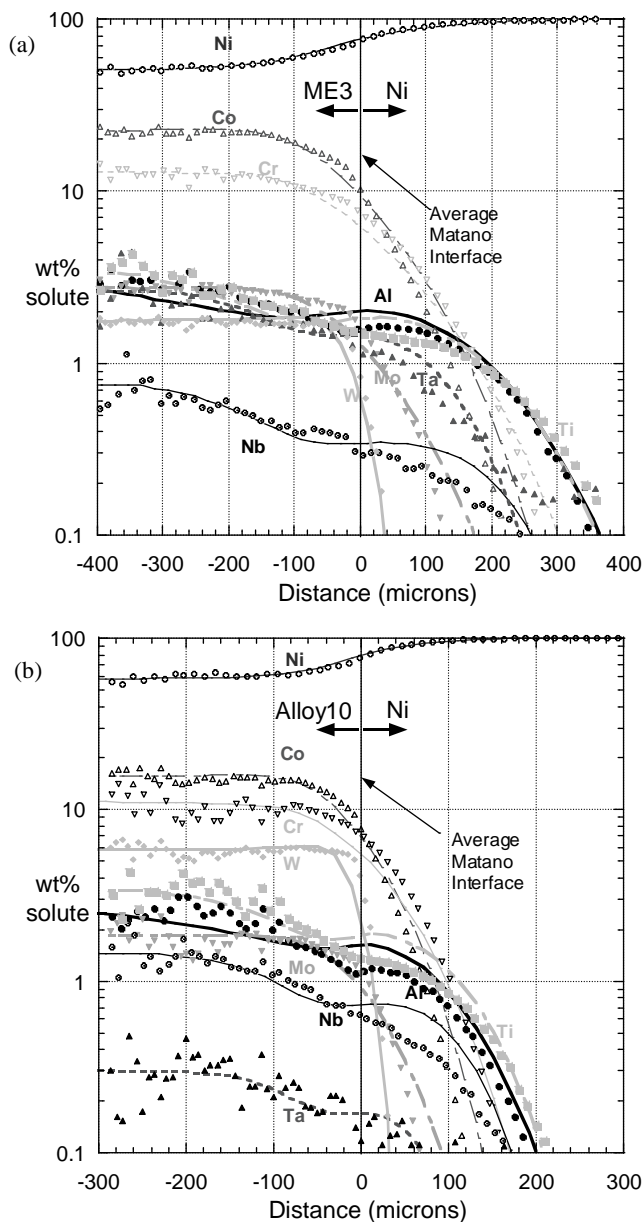


Figure 3 Comparison of microanalysis (discrete points) and DICTRA (curves) predicted composition trace of (a) ME3/Ni diffusion couple aged at 1093°C for 300 hr, and (b) Alloy10/Ni diffusion couples aged at 1093°C for 100 hr.

The agreement with the experimental microanalysis results is best using Ni-DATA 7 and NIST mobility databases. However, there are two discrepancies: (1) with the exception of Al, the experimental data does not confirm the predicted strong nonmonotonic profiles near the interface, and (2) the actual diffusion of Nb, Ta, Al, and Ti is less than predicted. Using the NIST mobility database with minor adjustments to the diffusivity prefactors of Cr, Nb and Ti (by factors of 1.4, 0.53 and 0.70, respectively), the predicted DICTRA composition profiles agree reasonably well with the microanalysis, as shown in two of the selected examples in Figure 3. However, comparative simulations

reveals that these adjustments do not affect the  $\gamma'$  precipitation simulation with *PrecipiCalc*. Hence, we conclude there is no correction needed to the NIST mobility database and thus  $D_{\text{scale}}$  is set to 1.

Furthermore, as seen in the micrograph of Figure 4(b), the width of significant grain growth in ME3 due to MC/ $\gamma'$  dissolution also agrees well with the DICTRA predicted phase fraction distribution in Figure 4(a).

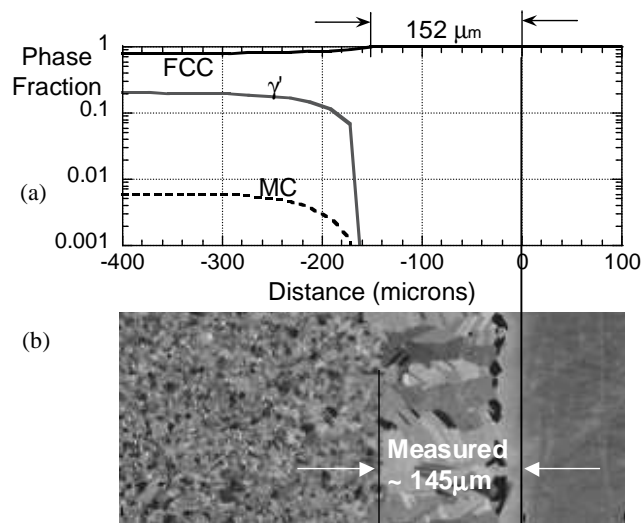


Figure 4 Comparison of (a) predicted equilibrium phase fractions, and (b) measured phase boundaries with adjusted Matano interface, for ME3/Ni 1093°C/100hr diffusion couple sample.

## Nonisothermal Precipitation

### Nucleation Onset Temperatures and SSDTA

As an efficient experimental check of nucleation behavior, transformation onset temperatures were measured in rapidly cooled arc melted samples of ME3 and Alloy10 using a Single Sensor Differential Thermal Analysis (SSDTA) technique developed at Ohio State University [15]. From nucleation theory, the most important material parameters affecting the nucleation rate are driving force (which is determined by the bulk thermodynamics), surface energy and elastic coherency energy. In this section, utilizing the Ni-DATA 7 and NIST mobility database, we present the results of calibrating the surface energy, while initially ignoring the coherency elastic energy.

The transformation onset temperatures ( $T_{\text{onset}}$ ) from the SSDTA experiments were determined from SSDTA data processing software, which takes the measured temperature versus time, fits the baseline prior to the transformation with a choice of function suitable for describing cooling, and then determines the departure point of measured data from the fitted function. The calibration of the SSDTA thermocouples has shown an accuracy of  $\pm 4.5^\circ\text{C}$  [16] in the relevant temperature range. To determine the onset temperature from *PrecipiCalc* simulation with physically

equivalent interpretation as closely as possible to the SSDTA results, the following summarizes our procedure.

- Process SSDTA measured temperature profiles to remove the latent heat contribution;
- Calculate material compositions relevant to the  $\gamma'$  precipitation from matrix  $\gamma$  phase — the high temperature phases (borides, carbides and undissolved  $\gamma'$ ) are removed with equilibrium calculations at highest SSDTA measured temperatures using the Ni-DATA 7 database.
- Perform *PrecipiCalc* simulations using Ni-DATA 7 and NIST mobility databases, with estimated surface energy;
- Collect time (or temperature) evolution results of  $\gamma'$  volume fraction, and compositions of matrix and  $\gamma'$ , compute the time (or temperature) evolution of molar enthalpy;
- Compute temperature derivatives of the molar enthalpy with respect to temperature,  $dH/dT$ ;
- Determine the transformation onset temperature where  $dH/dT$  changes by more than 10% of average  $dH/dT$  values, with decreasing temperature.

We note the difference of calculated  $T_{\text{onset}}$  values with the above enthalpy change approach and a simple approach of using a small  $\gamma'$  volume fraction of 0.1% is within the SSDTA accuracy.

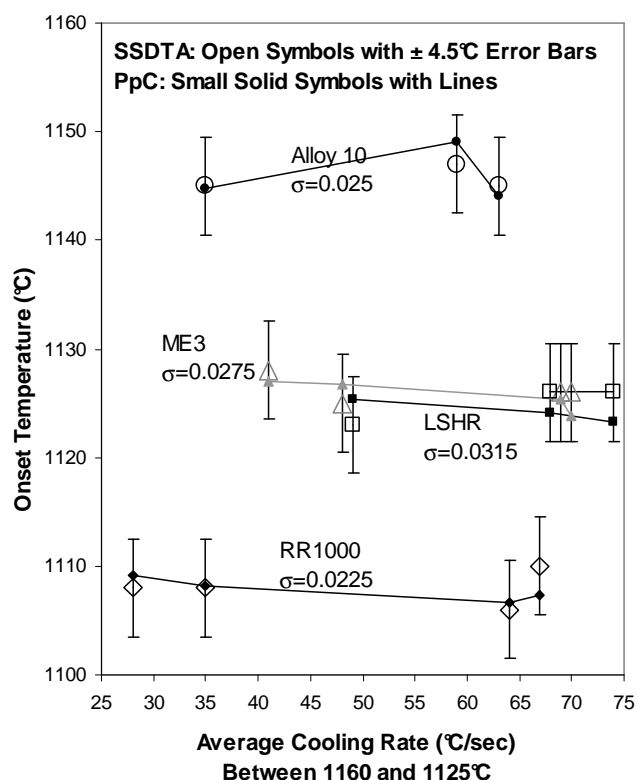


Figure 5 Summary of SSDTA results and *PrecipiCalc* (PpC) predictions with calibrated coherent interfacial energy  $\sigma_{\text{coh}}$  (values in  $\text{J/m}^2$ ). The data are plotted with respect to average cooling rate from measured temperature profiles.

Figure 5 summarizes the interfacial energy calibrated *PrecipiCalc* results and comparison to the SSDTA measured  $T_{\text{onset}}$ , for all 4 alloy samples. We varied the surface energy within 0.0225 to 0.0325  $\text{J/m}^2$ , and Figure 5 shows the best fit surface energy and  $T_{\text{onset}}$  results with minimum RMS of the difference between prediction and measurement. Except LSHR (which will be further discussed later), the optimized interfacial energies of the remaining three alloys are similar and agrees with the value of interfacial energy, 0.022~0.023  $\text{J/m}^2$ , reported by Sudbrack *et.al.* [9] for the Ni-Al-Cr ternary model alloys.

The experimental uncertainty of  $T_{\text{onset}}$  associated with SSDTA is represented by error bars in Figure 5. The *PrecipiCalc* predictions with optimized interfacial energy agree with SSDTA results well, and mostly fall within the experimental uncertainty. Note that the  $T_{\text{onset}}$  temperatures, both measured and predicted, do not monotonically decrease with the average cooling rate between 1125 to 1160°C. If the temperature followed linear cooling,  $T_{\text{onset}}$  should have decreased monotonically with higher cooling rate. The actual local temperature profile clearly affected the measured  $T_{\text{onset}}$ , and *PrecipiCalc* predictions capture the non-monotonic behavior very well.

Due to a furnace temperature limitation of the SSDTA experiment, Alloy10, having the highest predicted  $\gamma'$  solvus temperature, contains undissolved large  $\gamma'$  as confirmed by SEM (Figure 6). The observed amount is in good agreement with predicted equilibrium  $\gamma'$  fraction at the highest sample temperature in the furnace. The calculated  $T_{\text{onset}}$  of Alloy10 presented in Figure 5 was based on the assumption that undissolved  $\gamma'$  does not grow during the quench, allowing us to remove the large  $\gamma'$  completely in the *PrecipiCalc* simulations. To test this assumption, we performed an Alloy10 simulation allowing primary  $\gamma'$  growth during the quench, which resulted in a small reduction of nucleation onset temperature by only 1.6°C. Hence, we conclude the assumption to remove large undissolved  $\gamma'$  in SSDTA Alloy 10 quench simulation is reasonable.

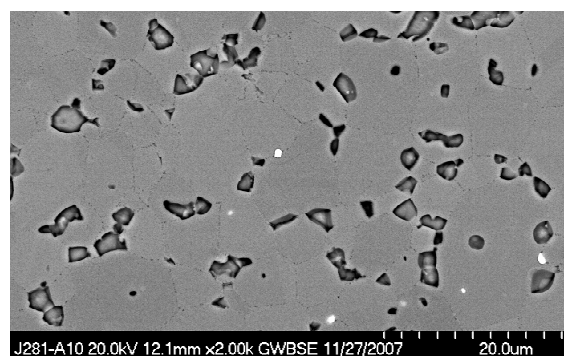


Figure 6 NASA SEM observation of an Alloy10 SSDTA sample.  $\gamma'$  volume fraction was estimated to be around 9.5%, which is compatible with Ni-DATA 7 equilibrium prediction of 8.4%  $\gamma'$  phase.

The relative ranking of best-fitting interfacial energies in Figure 5 ranks with the relative experimental nucleation undercoolings. This in turn ranks with the relative predicted misfit (RR1000 lowest, LSHR highest). Incorporation of a coherency elastic



energy  $G_{el}$  in further modeling will likely reduce the range of the coherent  $\sigma$  values. Using the surface energy of  $0.0225 \text{ J/m}^2$ , found for RR1000 and assumed to correspond to zero misfit, we reran *PrecipiCalc* for ME3, LSHR and Alloy 10 for SSDTA simulations with the same surface energy and then estimated the coherency elastic energy  $G_{el}$  by fitting to the measured nucleation onset temperature. Table 9 summarizes the results, and also the corresponding at-temperature misfits based on the theoretical elastic strain energy of inclusions [17]. According to this analysis, LSHR corresponds to the highest misfit, followed by ME3 and Alloy 10, in a similar ranking but at about 1/3 of the misfit values of the model prediction in Figure 1. These misfit estimates will be validated against ongoing XRD experiments. In subsequent *PrecipiCalc* simulation to be discussed here, the surface energies in Figure 5 are used.

Table 9 Elastic energy based misfit estimate from SSDTA nucleation onset temperatures and RR1000 surface energy.

	Estimated $G_{el}$ (J/mole)	Misfit (%)
RR1000	0	0
Alloy 10	30	0.5
ME3	50	0.61
LSHR	80	0.8

#### $\gamma'$ Microstructure in SSDTA Samples

The well-defined thermal history of the SSDTA samples also provides an excellent opportunity for experimental validation of *PrecipiCalc* simulations of nonisothermal precipitation. Using LEAP APT, we analyzed the ME3 Ar gas-quenched sample (ME3-1Ar) from the SSDTA experiment. In total, 32 million atoms were analyzed. The overall bulk composition is very close to the expected composition. Larger  $\gamma'$  precipitates, about 40-60nm in diameter, were observed together with ultrafine  $\gamma'$  precipitates, about 5nm or less in diameter.

High-resolution SEM (HR SEM) analysis was also conducted on the same ME3-1Ar SSDTA sample, as well as an LSHR Ar gas-quenched sample (LSHR-2Ar). Consistent results between the APT and SEM for ME3-1Ar are shown in Figure 7. As shown by the higher magnification views at the bottom of Figure 7, fine  $\gamma'$  formed at lower temperature during SSDTA cooling was also observed in both ME3-1Ar LEAP APT and HR SEM.

Table 10 shows a summary of measured larger  $\gamma'$  size and also *PrecipiCalc* predictions using the measured SSDTA temperature profiles. *PrecipiCalc* provides reasonable estimates with the approximations employed thusfar. Figure 8 shows reasonable agreement in particle size histograms between HR SEM and simulation for the LSHR-2Ar sample. In RR1000-3He (He gas-quenched) LEAP study, fraction of 35% was determined for largest  $\gamma'$ , which agrees well with *PrecipiCalc*'s 37.6%.

As in the case of the model alloy of Table 8, the APT measurements in the ME3-1Ar sample show W partitioning in the direction of thermodynamic prediction for the larger  $\gamma'$  population. However, the W profiles observed for the ultrafine population suggest solute trapping of the slowest diffusing

components may be occurring during precipitation at the lowest temperatures.

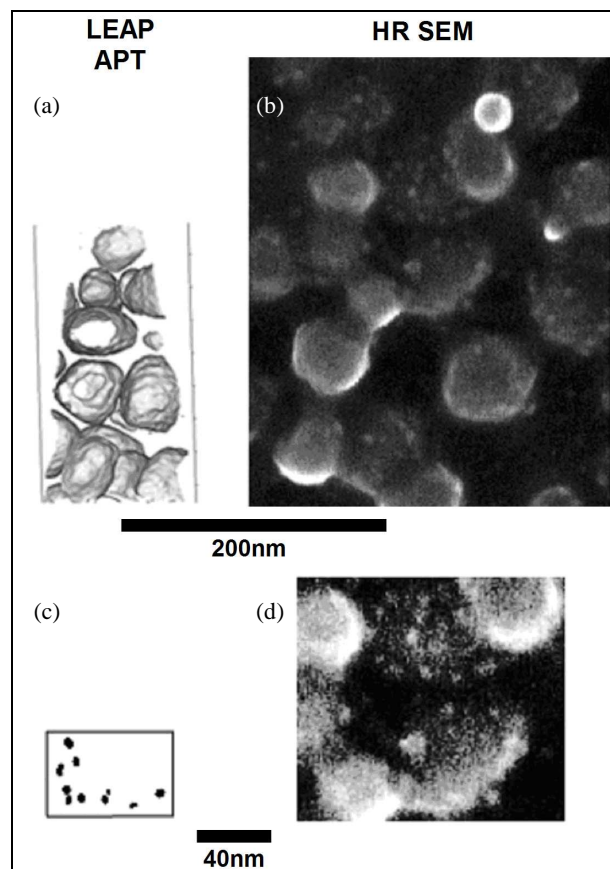


Figure 7 Characterization of  $\gamma'$  microstructure in ME3-1Ar SSDTA sample. Left (a,c) figures from LEAP APT and right (b,d) figures from HR-SEM are compared at two different length scale — (a) and (b) at smaller magnification, showing larger  $\gamma'$ , and (c) and (d) at slightly higher magnification showing very fine  $\gamma'$ .

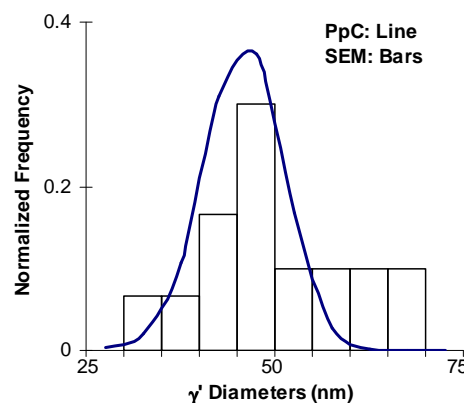


Figure 8 Comparison of particle size histogram of *PrecipiCalc* (3D results) and HR SEM with an observation of 30  $\gamma'$  particles in an LSHR-2Ar SSDTA sample.

Table 10 Comparison of the largest  $\gamma'$  mean diameters between two SSDTA samples and *PrecipiCalc* simulation using the coherent interfacial energies discussed previously.

	LEAP APT	HR SEM	<i>PrecipiCalc</i> Predictions
ME3-1Ar	40-60 nm	53.8 nm	41 nm
LSHR-2Ar	-	50.1 nm	45.6 nm
RR1000-3He	20-45 nm	31.8 nm	20.5 nm

# $\gamma'$ Microstructure in ME3 Water Quenched Samples

LEAP APT microanalysis was conducted on ME3 samples water quenched from both subsolvus treatment at 1093°C (1000hr) and supersolvus treatment at 1200°C (1hr). For the supersolvus treated sample, a LEAP dataset containing 8.7 million atoms within a box of 128×55×54 nm<sup>3</sup> was collected. The LEAP data analysis shows nanoscale  $\gamma'$  precipitates of about 15~30nm in diameter, which is in good agreement with our *PrecipiCalc* prediction of 30nm with an estimated cooling temperature profile. TEM work at NASA GRC indicates a larger mean diameter of  $\gamma'$  at 44nm.

For the 1093°C subsolvus treated ME3, the LEAP experiment used to obtain 1093°C matrix composition (Table 3) was further analyzed for fine quench  $\gamma'$ . An estimated 10-20nm effective diameter from LEAP APT is in reasonable agreement with the predicted 29nm diameter from *PrecipiCalc* simulation with an estimated cooling temperature profile. A proximity histogram of the subsolvus LEAP sample summarizes the measured partitioning of solutes between the  $\gamma$  and  $\gamma'$  phases in Figure 9. As summarized in Table 11 for both subsolvus and supersolvus treated samples, the partitioning is again in the direction of thermodynamic prediction, with the notable exception of the flat W profile offering further evidence that the slowest diffusing component exhibits solute trapping at extreme cooling conditions. Further study will address whether solute trapping need be considered for industrially-relevant processing conditions.

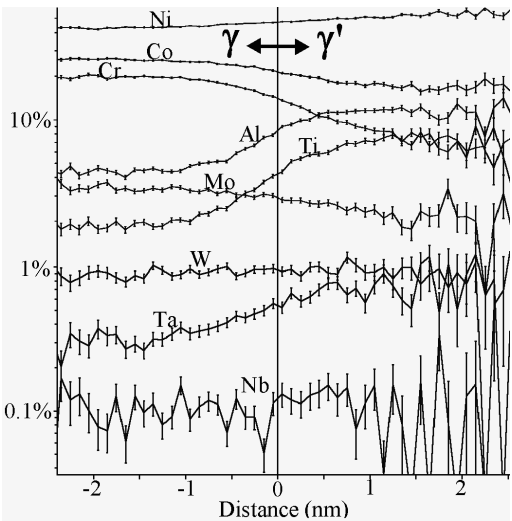


Figure 9  $\gamma$  and fine quench  $\gamma'$  compositions (in atomic %) analysis of LEAP experiment on ME3 1093°C/1000hr isothermal hold sample.

Table 11 Comparison of measured nanoscale  $\gamma'$  particle and matrix compositions in ME3 with corresponding *PrecipiCalc* simulations.

ME3		Compositions, at%									RMS
		Ni	Al	Cr	Co	Ti	Mo	W	Nb	Ta	
Subsolvus											2.80
$\gamma$	APT	42.5	4.9	21.3	23.7	2.3	3.6	1.0	0.4	0.3	
	PpC	35.0	2.82	27.3	27.7	0.51	5.28	1.30	0.07	0.08	
$\gamma'$	APT	55.6	9.3	7.3	17.5	6.1	2.1	0.8	0.4	0.8	3.07
	PpC	61.3	12.8	2.1	12.2	8.2	0.42	0.52	1.2	1.2	
Supersolvus											1.71
$\gamma$	APT	40.5	4.8	22.5	23.8	2.0	4.2	0.8	0.6	0.5	
	PpC	39.2	3.00	24.6	27.5	0.74	3.94	0.87	0.08	0.13	
$\gamma'$	APT	56.5	12.0	3.5	13.6	8.9	1.9	0.5	1.0	1.6	1.01
	PpC	62.2	12.4	1.94	11.9	8.50	0.32	0.34	1.0	1.3	

# $\gamma'$ Microstructure in Furnace Cooled Samples

Supersolvus treated ME3, LSHR and Alloy10 samples followed by instrumented furnace cooling were characterized under SEM. The cooling rate between 1160 and 1125 °C is around 0.54C/sec, which is about two orders of magnitude slower than the SSDTA and water quench experiments. These experiments offer growth-dominated conditions for calibration of interfacial mobility. *PrecipiCalc* simulations were conducted using the coherent surface energies determined from the SSDTA study and the individually measured temperature cooling profiles for each samples. The *PrecipiCalc* 3D results converted to 2D are in reasonable agreement with the SEM results, as shown in Table 12. Unlike the finer  $\gamma'$  particles formed during SSDTA fast cooling (see Figure 8) which were etched to reveal 3D sizes in SEM,  $\gamma'$  particles here are much larger and should be compared to the 2D results. As shown in Figure 10, we observe reasonable agreement between simulation and experimental size distribution for these growing supercritical  $\gamma'$  particles, showing sharper size distribution than that from coarsening theory. Note the truncation of the calculated 2D distribution is 10nm, which is about the resolution of SEM and image analysis.

These *PrecipiCalc* simulations were carried out with coherent  $\gamma/\gamma'$  surface energy and without interfacial dissipation ( $M_o$  term in Table 2). Though these  $\gamma'$  particles are significantly larger than those found in SSDTA and water quench experiments, there is no indication that they are incoherent with the matrix. However, it is possible that they are semi-incoherent and are in the process of losing coherency.

Table 12 Comparison of the largest  $\gamma'$  mean sizes (diameters) between furnace cooled samples and *PrecipiCalc* simulations.

	HR SEM	<i>PrecipiCalc</i> Results converted to 2D
ME3	430 nm	348 nm
LSHR	408 nm	402 nm
Alloy 10	376 nm	396 nm



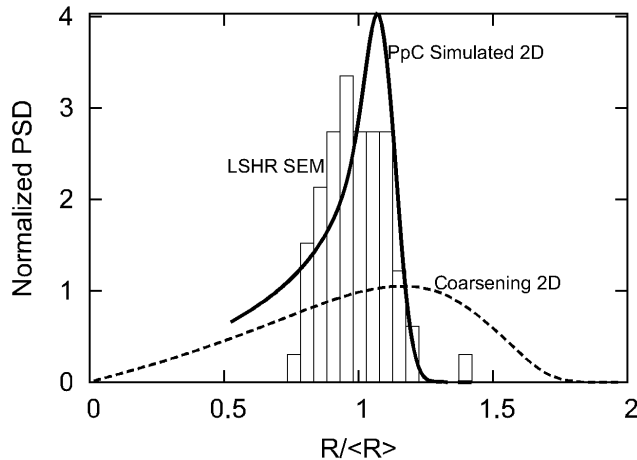


Figure 10 Comparison shows good agreement between experimental SEM (bars) and *PrecipiCalc* simulated (converted to 2D, solid line) and normalized particle size distributions for LSHR furnace cooled sample. 2D coarsening size distribution is shown in a dash line.

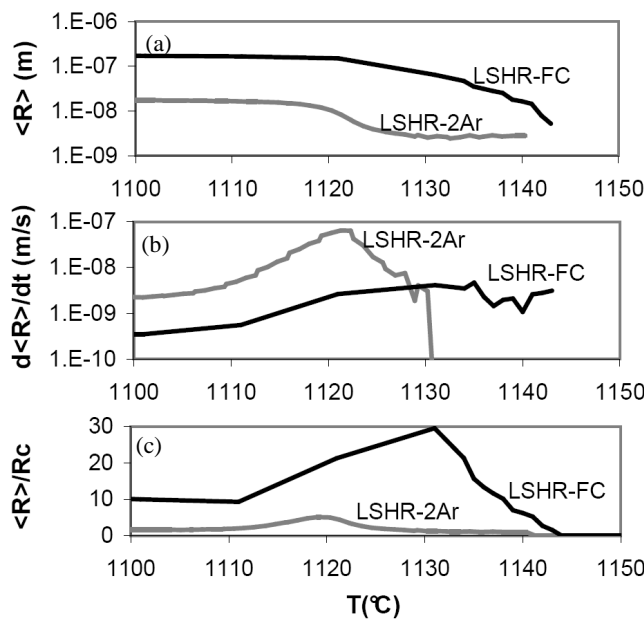


Figure 11 Comparison of *PrecipiCalc* simulated  $\gamma'$  (a) mean radius ( $\langle R \rangle$ ), (b) growth rate and (c) mean radius over critical radius ( $R_c$ ) ratio with respect to temperatures for both LSHR furnace cooled (FC) and SSDTA (2Ar). In this temperature range, only the first  $\gamma'$  distribution is formed in these two calculations.

Figure 11 compares the *PrecipiCalc* simulated  $\gamma'$  size and growth rate evolution of fast cooled SSDTA and slow furnace cooled LSHR samples. In these two very distinct cooling rates,  $\gamma'$  nucleates at similar sizes within a narrow temperature window (1140~1142°C). In the slower furnace cooled case (LSHR-FC), nucleated  $\gamma'$  particles can grow to much higher multiples of critical size (Figure 11c), despite the slower growth rate (due to lower supersaturation in slower cooling) compared to the fast cool at temperatures below 1130°C (Figure 11b). This dominance of

growth leads to the sharper size distribution of Figure 10. The good agreement with average size in Table 12 suggests that interfacial dissipation can be neglected for particle size up to the 500nm scale.

### Coarsening Experiments

ME3, LSHR and Alloy10 samples were supersolvus treated at 1193°C for 1 hr, water quenched, and then aged at different conditions, followed by a water quench. The aging conditions selected are 1093°C for 20 and 1000 hr, 927°C for 1000 hr, and 760°C for 1000 hr. The samples were then analyzed under TEM or SEM, depending on the size scale of  $\gamma'$  particles. For higher temperature aging, both intragranular  $\gamma'$  and grain boundary  $\gamma'$  particles are monitored as represented in in Figure 12. Similar to Alloy 10 in Figure 2a, the intragranular  $\gamma'$  in ME3 shows an ordered alignment, indicating coherency based elastic interaction. A consistent image processing technique was used to identify the grain boundary  $\gamma'$  and to obtain the sizes and fractions of both types of  $\gamma'$  particles for all ME3, LSHR and Alloy 10 samples. All of these heat treatment and experimental analysis were conducted at NASA GRC.

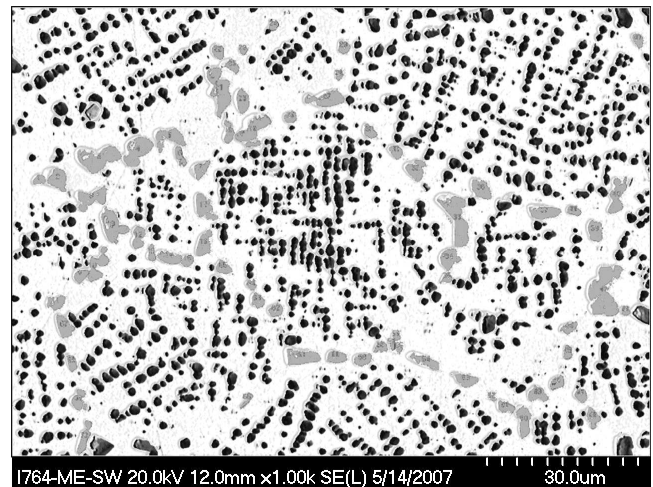


Figure 12 SEM image (processed to show different features) of ME3 supersolvus treated and then aged at 1093°C for 1000hr. Intragranular and grain boundary  $\gamma'$  are represented as black and grey, respectively.

Table 13 summarizes the measured  $\gamma'$  sizes in these heat treatment conditions. The grain boundary  $\gamma'$  particles are typically larger than the intragranular  $\gamma'$  particles by a factor of 1.5 to 2. Between ME3, LSHR and Alloy 10, there are no consistent trends in the relative  $\gamma'$  sizes. We note that the TEM and SEM measured sizes correspond to the mean 3D and 2D sizes, respectively.

The *PrecipiCalc* modeling of coherent intragranular  $\gamma'$  in these isothermally aged coarsening experiments is ongoing. Program plans include the modeling of incoherent grain boundary  $\gamma'$  using *PrecipiCalc*'s heterogeneous grain boundary nucleation model. The grain boundary  $\gamma'$  growth simulations will include effects of grain boundary diffusion and possibly interfacial mobility to account for incoherent interfaces.

Table 13 Summary of experimental measured  $\gamma'$  mean equivalent diameters ( $\mu\text{m}$ ) of isothermally aged samples. Intragranular (G)  $\gamma'$  and grain boundary (GB)  $\gamma'$ , when observed, are reported separately.

Aging Conditions	Exp	ME3		LSHR		Alloy 10	
		G	GB	G	GB	G	GB
Before Aging	TEM	0.044	-	0.028	-	0.044	-
1093C-20h	SEM	0.510	0.810	0.504	0.984	0.546	1.084
1093C-1000h	SEM	1.380	2.840	1.420	2.996	0.894	2.618
927C-1000h	SEM	0.584	0.758	0.598	0.954	0.670	1.224
760C-1000h	TEM	0.058	-	0.062	-	0.062	-

### Conclusion and Summary

Measured  $\gamma$ - $\gamma'$  phase compositions in equilibrated 3<sup>rd</sup> generation disc alloys and reported phase compositions in simple Ni-Cr-Al-X model alloys show best agreement with the ThermoTech Ni-Data version 7 thermodynamic database. In the context of multicomponent disc alloys, the assessed sensitivity of predicted phase fractions, APB enthalpy and interphase misfit to measured composition error is judged as acceptable within current structure/property model uncertainty. Prediction of a relatively high misfit in the high-refractory 3<sup>rd</sup> generation alloys is supported by microstructural evidence, but precise predictions will require further misfit model calibration. Comparison of measured composition profiles in diffusion couples of ME3 and Alloy 10 with pure Ni against DICTRA multicomponent diffusion simulations indicates the combination of the Ni-DATA version 7 thermodynamic database with the NIST mobility database gives sufficient accuracy to support *PrecipiCalc* simulation of diffusional precipitation without diffusivity modification. The SSDTA measurement of critical nucleation undercoolings defines reasonable values of coherent interfacial energies. Incorporation in *PrecipiCalc* simulation of nonisothermal precipitation for both supersolvus and subsolvus treated materials gives good agreement with observed particle sizes and compositions. APT microanalysis shows some evidence of solute trapping of W, the slowest diffusing component, in fine precipitates forming at extreme cooling rates. Further modeling of measured long-term coarsening behavior requires refinement of coherency elastic energy estimates and treatment of the parallel evolution of incoherent precipitation at grain boundaries. The accuracy of predictions validated so far indicates that available fundamental databases and precipitation models offer sufficient fidelity for effective application of the AIM methodology to the accelerated optimization of hybrid thermal processing of 3<sup>rd</sup> generation aeroturbine disc alloys.

### Acknowledgement

This work is supported by NASA Aviation Safety Program and Glenn Research Center (GRC) under Contract No. NNC07CB01C. The authors acknowledge John Gayda and Tim Gabb of NASA GRC for project collaboration and experimental work, Jeff Simmons and Chris Woodward of the Air Force Research Laboratory for serving as science advisors of this program, David Furrer, Rob Mitchell and Mark Hardy of Rolls-Royce Corporation for serving as industrial advisors of this program, Carelyn Campbell of NIST for providing the mobility database, Boian Alexandrov of Ohio State University for SSDTA

work, Chris Kern and Sean Backs of QuesTek for SEM characterization and analysis, S.-L. Chen of CompuTherm and Paul Mason of Thermo-Calc AB for assisting thermodynamics calculation, Howard Stone of University of Cambridge for RR1000 data, Eugene Kang of Northwestern University for SEM data analysis, and David Seidman of Northwestern University for discussion and suggestions on LEAP APT results.

### References

1. H.-J. Jou, P. Voorhees and G.B. Olson, "Computer Simulations for the Prediction of Microstructure/Property Variation in Aeroturbine Disks," *Superalloys 2004*, Eds K.A. Green, T.M. Pollock, H. Harada, T.E. Howson, R.C. Reed, J.J. Schirra, and S. Walston, 2004, 877-886.
2. A.M. Wusatowska-Sarnek, G. Ghosh, G.B. Olson, M.J. Blackburn, and M. Aindow, "A Characterization of the Microstructure and Phase Equilibria Calculations for the Powder Metallurgy Superalloy IN100," *J. Materials Research*, 18 (2003), 2653-2663.
3. <http://www.thermocalc.com/Products/TCC.html>
4. <http://www.thermocalc.com/Products/Dictra.html>
5. N. Saunders, M. Fahrman and C.J. Small, "The Application of CALPHAD Calculations to Ni-Based Superalloys," *Superalloys 2000*, eds. K.A. Green, T.M. Pollock and R.D. Kissinger, (TMS, Warrendale, 2000), 803.
6. <http://www.compuTherm.com/databases.html>
7. Database provided by Dr. Ursula Kattner at NIST.
8. <http://www.thermocalc.com/Products/Databases/TCN11.htm>
9. C.K. Sudbrack, D. Isheim, R.D. Noebe, N.S. Jacobson, and D.N. Seidman, "The Influence of Tungsten on the Chemical Composition of a Temporally Evolving Nanostructure of a Model Ni-Al-Cr Superalloy," *Microsc. Microanal.*, 10 (2004), 355-365.
10. C.K. Sudbrack, T.D. Ziebell, R.D. Noebe, D.N. Seidman, "Effects of a tungsten addition on the morphological evolution, spatial correlations and temporal evolution of a model Ni-Al-Cr superalloy," *Acta Materialia*, 56 (2008) 448-463.
11. C.K. Sudbrack, R.D. Noebe, and D.N. Seidman, "Compositional pathways and capillary effects during isothermal precipitation in a nondilute Ni-Al-Cr alloy," *Acta Materialia*, 55 (2007), 119-130.
12. K.E. Yoon, R.D. Noebe, and D.N. Seidman, "Effects of rhenium addition on the temporal evolution of the nanostructure and chemistry of a model Ni-Cr-Al superalloy. II: Analysis of the coarsening behavior," *Acta Materialia*, 55 (2007), 1145-1157.
13. A.P. Miodownik and N. Saunders, *Applications of Thermodynamics in the Synthesis and Processing of Materials*, ed. Nash and Sundman, TMS, (1995) 91.
14. C.E. Campbell, W.J. Boettinger, and U.R. Kattner, *Acta Materialia*, 50 (2002) 775-792.
15. B.T. Alexandrov and J.C. Lippold, "Single Sensor Differential Thermal Analysis of Phase Transformations and Structural Changes during Welding and Postweld Heat Treatment," *Welding in the World*, 51, 11/12 (2007) 48-59 (Doc. IIW 1843-07).
16. Private communication with B. Alexandrov, Ohio State University, 2008.
17. T. Mura, *Micromechanics of Defects in Solids*, 2nd Edition, Kluwer Academic, 1987.